AFRL-RX-WP-JA-2017-0424

PASSIVATION OF DEFECTS IN MONOLAYER MOS2 – IN SITU PHOTOLUMINESCENCE AND RAMAN STUDIES (PREPRINT)

Rahul Rao and Ahmad E. Islam
UES, Inc.

Benji Maruyama
AFRL/RX

Victor Carozo, Nestor Perea-Lopez, and Mauricio Terrones
Pennsylvania State University

3 August 2017
Interim Report

(STINFO COPY)

AIR FORCE RESEARCH LABORATORY
MATERIALS AND MANUFACTURING DIRECTORATE
WRIGHT-PATTERSON AIR FORCE BASE, OH 45433-7750
AIR FORCE MATERIEL COMMAND
UNITED STATES AIR FORCE

REPORT DOCUMENTATION PAGE

Form Approved
OMB No. 0704-0188

1. REPORT DATE *(DD-MM-YY)*	2. REPORT TYPE	3. DATES COVERED *(From - To)*
3 August 2017	Interim	8 September 2014 – 3 July 2017

4. TITLE AND SUBTITLE
PASSIVATION OF DEFECTS IN MONOLAYER MOS2 – IN SITU PHOTOLUMINESCENCE AND RAMAN STUDIES (PREPRINT)

5a. CONTRACT NUMBER
FA8650-15-D-5405-0002

5b. GRANT NUMBER

5c. PROGRAM ELEMENT NUMBER

6. AUTHOR(S)
1) Rahul Rao and Ahmad E. Islam – UES
2) Benji Maruyama - AFRL/RX
(continued on page 2)

5d. PROJECT NUMBER

5e. TASK NUMBER 0002

5f. WORK UNIT NUMBER
X0YE

7. PERFORMING ORGANIZATION NAME(S) AND ADDRESS(ES)
1) UES, Inc.
4401 Dayton Xenia Rd.
Beavercreek, OH 45432
2) AFRL/RX
Wright-Patterson AFB
Dayton, OH 45433
(continued on page 2)

8. PERFORMING ORGANIZATION REPORT NUMBER

9. SPONSORING/MONITORING AGENCY NAME(S) AND ADDRESS(ES)
Air Force Research Laboratory
Materials and Manufacturing Directorate
Wright-Patterson Air Force Base, OH 45433-7750
Air Force Materiel Command
United States Air Force

10. SPONSORING/MONITORING AGENCY ACRONYM(S)
AFRL/RXAS

11. SPONSORING/MONITORING AGENCY REPORT NUMBER(S)
AFRL-RX-WP-JA-2017-0424

12. DISTRIBUTION/AVAILABILITY STATEMENT
Distribution Statement A. Approved for public release: distribution unlimited.

13. SUPPLEMENTARY NOTES
PA Case Number: 88ABW-2017-3807; Clearance Date: 3 Aug 2017. This document contains color. The U.S. Government is joint author of the work and has the right to use, modify, reproduce, release, perform, display, or disclose the work.

14. ABSTRACT *(Maximum 200 words)*
Lattice defects impact the optoelectronic properties of monolayer transition metal dichalcogenides (TMDs). In particular, chalcogen vacancies are the most prevalent lattice defect in monolayer TMDs synthesized by chemical vapor transport methods. In the case of monolayer MoS2, sulfur vacancies create mid-gap states and render the material electron-rich. Passivation of these defects by acceptor molecules is an attractive way to recover the optical properties. Here we study passivation of lattice defects in monolayer MoS2 by oxygen. Using both photoluminescence and Raman spectroscopy, we extract electron densities due to sulfur vacancies. We then study the kinetics of passivation of these defects using in situ PL and Raman spectroscopy at room temperature and at 77K. The passivation results in a blueshift of the PL and reduction in electron density, and the kinetics curves are well fit with a double exponential (two time constants). The first (shorter) time constant is a result of cleaning of the surface of MoS2 by the irradiation laser, and the second (longer) time constant corresponds to oxygen bonding on to the MoS2. Our study shows that passivation of defects with oxygen is a viable and quick technique to enhance the optical performance of MoS2 for use in devices.

15. SUBJECT TERMS
Lattice defect; optoelectronic; transition metal dichalcogenide (TMD); monolayer MoS2; sulfer; Raman spectroscopy

16. SECURITY CLASSIFICATION OF:			17. LIMITATION OF ABSTRACT:	18. NUMBER OF PAGES	19a. NAME OF RESPONSIBLE PERSON (Monitor)
a. REPORT	b. ABSTRACT	c. THIS PAGE			Lawrence Brott
Unclassified	Unclassified	Unclassified	SAR	29	19b. TELEPHONE NUMBER *(Include Area Code)* (937) 255-9157

REPORT DOCUMENTATION PAGE Cont'd

6. AUTHOR(S)

3) Victor Carozo, Nestor Perea-Lopez, and Mauricio Terrones - PSU

7. PERFORMING ORGANIZATION NAME(S) AND ADDRESS(ES)

4) Pennsylvania State University
201 Old Main, University Park, PA 16802

Passivation of Defects in Monolayer MoS_2 – In situ Photoluminescence and Raman Studies

Rahul Rao,[1,2,*] Victor Carozo,[3,4] Ahmad E. Islam,[1,2] Nestor Perea-Lopez,[3] Mauricio Terrones,[3,4,5] Benji Maruyama[1]

[1]Materials and Manufacturing Directorate, Air Force Research Laboratory, Wright-Patterson AFB, OH 45433, USA

[2]UES Inc., Dayton, OH 45432, USA

[3]Department of Physics and Center for Two-Dimensional and Layered Materials, The Pennsylvania University, State College, PA

[4]Department of Materials Science and Engineering, The Pennsylvania State University, University Park, PA 16802, USA

[5]Department of Chemistry, The Pennsylvania State University, University Park, PA 16802, USA.

*Correspondence: rahul.rao.ctr.1@us.af.mil

Abstract

Lattice defects impact the optoelectronic properties of monolayer transition metal dichalcogenides (TMDs). In particular, chalcogen vacancies are the most prevalent lattice defect in monolayer TMDs synthesized by chemical vapor transport methods. In the case of monolayer MoS_2, sulfur vacancies create mid-gap states and render the material electron-rich. Passivation of these defects by acceptor molecules is an attractive way to recover the optical properties. Here we study passivation of lattice defects in monolayer MoS_2 by oxygen. Using both photoluminescence and Raman spectroscopy, we extract electron densities due to sulfur vacancies. We then study the kinetics of passivation of these defects using *in situ* PL and Raman spectroscopy at room

temperature and at 77K. The passivation results in a blueshift of the PL and reduction in electron density, and the kinetics curves are well fit with a double exponential (two time constants). The first (shorter) time constant is a result of cleaning of the surface of MoS_2 by the irradiation laser, and the second (longer) time constant corresponds to oxygen bonding on to the MoS_2. Our study shows that passivation of defects with oxygen is a viable and quick technique to enhance the optical performance of MoS_2 for use in devices.

Introduction

Monolayer 2D transition metal dichalcogenides (TMDs) exhibit bright photoluminescence emission (PLE) that makes them attractive for use as photoemitters; their form factor is especially suitable for flexible electronic applications.[1-3] The emission comes from a radiative recombination of excitons across a direct bandgap in the visible range of the electromagnetic spectrum, and is several orders of magnitude brighter than the PLE from their bulk counterparts.[4,5] However, the emission can be drastically reduced in the presence of lattice defects through non-radiative recombination, limiting the quantum yield of the material.[6]

Lattice defects exist mainly in the form of chalcogen vacancies in monolayer TMDs, and have been observed in relatively high quantities (up to 3 x 10^{13} cm^{-2} or 3 at.%) in monolayer crystals grown by chemical vapor deposition (CVD).[7,8] Other defects include metal vacancies, grain boundaries, tilt boundaries and dislocations,[7] all of which can mediate the non-radiative recombination of excitons, diminishing the PL intensity from the monolayer TMDs. These defects also modulate the charge carrier density within the TMD. In particular, it has been found that chalcogen vacancies render the TMD electron-rich, which manifests in an increase in the intensity of photo-excited charged excitons (also called trions) compared to neutral excitons.[9]

Arguably the easiest and most practical way to increase the quantum yield of a monolayer TMD is to electronically passivate the defects by charge transfer from adsorbed molecules. In the case of electron-rich TMDs, any electron acceptor species would therefore restore the balance of

charges within the layer. Indeed, a number of molecules such as thiols[10,11] and various acids[12-14] have been found to be effective at passivating defects in TMDs and improving their optoelectronic properties.

In addition to solvents, oxygen has been shown to also be effective at enhancing the PL intensity of exfoliated and CVD-grown MoS_2 and other TMDs.[15-20] The enhancement by oxygen adsorption is of particular interest because of its simple and practical applicability for a variety of TMDs. Oxygen adsorption and bonding induces p-type doping in MoS_2[15,17,19,21] and other layered materials,[20,22,23] and is reportedly enhanced in the presence of laser irradiation.[17,20] The enhancement of PL by laser irradiation is particularly attractive because of the potential for patterning and modulating the charge density in the monolayer TMDs. However, the role of the laser with respect to photochemistry and the kinetics of the passivation process still remain to be explained in detail.

Here we perform a systematic *in situ* study to characterize lattice defects in monolayer MoS_2 and to understand the mechanism of passivation upon laser irradiation. Our measurements are preformed on CVD-grown monolayer MoS_2 crystals on SiO_2 substrates that have been stored under ambient conditions for several months after synthesis. The ageing process has been shown to render monolayer TMDs with a high density of chalcogen vacancies and a loss of PL intensity.[23,24] While lattice defects in TMDs have been extensively characterized by electron microscopy,[7] here we use optical spectroscopy, in particular PL and resonance Raman spectroscopy to correlate the PL intensities and emission energies to defect densities. To do this we simultaneously measure the Raman and PL spectra from several crystals with both resonance (633 nm) and non-resonance (514 nm) excitation. By combining the PL and Raman measurements we are then able to extract electron densities. We then measure the kinetics of defect passivation at room temperature and at 77K for various laser power densities. We find the passivation to occur on two time scales with the whole process achieving completion within a few minutes: we attribute the first short time constant to removal of surface adsorbates by the laser,

and the second longer time constant to bonding of oxygen at the sulfur vacancy sites. Our systematic study shows for the first time the direct relationship between the electronic and phononic structure of the MoS_2, while at the same time provides valuable insights into the defect passivation process.

Results

Raman and PL characterization of defects

We start by measuring Raman and PL spectra from 40 different CVD-grown monolayer MoS_2 crystals on an SiO_2 substrate that has been aged in an ambient laboratory environment. As mentioned above, the aging process leads to the gradual removal of sulfur atoms, resulting in an increase in electron density and hence, intensity of trion emission compared to bi-exciton emission.[23,24] Figure 1a shows representative PL spectra collected with 514 nm excitation from two MoS_2 crystals (see Fig. S1a for PL spectra with 514 nm excitation from all the measured crystals). The asymmetric emission peak can be deconvoluted into two peaks with the higher energy peak at ~1.83 eV corresponding to bi-exciton emission (labeled *A*) and the lower energy peak at ~1.77 eV corresponding to trion emission (labeled A^-). The intensity of the A^- peak can be seen to vary with respect to the *A* peak between the two spectra; it is more intense in the bottom trace compared to the top trace. In addition, the PL emission in the bottom trace is redshifted, broadened and less intense than the top trace.

The variation of trion emission intensity and redshift of PL peaks over all the measured 40 crystals is captured in Figure 1c, which plots the ratio of intensities of the A^- to *A* peak (I_{A^-}/I_A) against average emission energy. Here for simplicity we measure the average emission energy by fitting the PLE to a single Lorentzian peak. Fig. 1c shows that the overall redshift in PL is correlated with increasing trion (A^-) emission. An increase in the A^- emission peak and redshift of the PLE corresponds to increased electron density,[25] which is presumably a result of increasing

sulfur vacancies. The maximum redshift of the emission peak is ~30 meV, and is comparable to other reported values of redshifted emission due to n-type doping.[25,26]

Figure 1b shows two representative PLE spectra collected using 633 nm excitation (see Fig. S1b for PL spectra with 633 nm excitation from all of the measured crystals). Similar to the spectra in Fig. 1a, the emission curves can be deconvoluted into *A* and A^- peaks, and exhibit similar I_{A^-}/I_A ratios and redshifted PLE. Importantly, the PL spectra collected from the same spot with both the 514 and 633 nm excitations correlate very well (Fig. S2), allowing us to freely compare between the two sets of data for each crystal. The reason why we choose 633 nm (1.96 eV) excitation is its closeness to the optical bandgap energy of monolayer MoS_2 (~1.83 eV).

The near-resonance excitation enables the observation of several non-zone center and combination Raman modes, as shown in the inset in Fig. 1b. The most prominent of these modes is an asymmetric peak at ~225 cm^{-1}, which arises from scattering of photons by *LA* phonons at the Brillouin zone boundaries. In the case of MoS_2, the *LA* phonon branch crosses both *M* and *K* points of the Brillouin zone at ~225 cm^{-1},[27] and this peak contains contribution from both phonons. However, for this discussion we label this peak as the *LA* peak and do not distinguish between *M* and *K* point phonons. The *LA* peak has been observed to increase in intensity due to lattice defects[28,29] and its intensity ratio with respect to the *E'* Raman peak ($I_{LA}/I_{E'}$) can be used as a measure of defect density.[21,30] It is clear in Fig. 1b that the *LA* peak intensity is higher in the bottom (red) trace compared to the top (blue) trace, suggesting a higher defect density in the bottom spectrum. This higher defect density also correlates with the increased trion emission in the crystals and is depicted in Fig. 1d, which shows the $I_{LA}/I_{E'}$ ratios plotted against the PLE energies. The data in Fig. 1c and 1d have been color coded so that direct comparisons can be made between the corresponding data points. Taken together, the data in Figs 1c and 1d show that increased trion emission and redshifted PL also corresponds to increased defect density. To our knowledge, this is the first time such a correspondence has been shown between the PL and

Raman spectra in any TMD, and it highlights the close relationship between the electronic and phononic band structure.

We next examine the frequencies of Raman peaks in the crystals. Under 514 nm excitation, MoS_2 exhibits two major vibrational peaks, *E*' and *A*', corresponding to in-plane and out-of-plane vibrations of the Mo and S atoms, respectively. We only analyze the Raman peak frequencies from the spectra collected with 514 nm excitation owing to the ease in peak fitting compared to the complex spectra collected with 633 nm excitation (inset in Fig. 1b). We find that the *A'* peak redshifts from ~404.5 to ~403 cm^{-1}, concomitantly with the redshift in the PLE (Fig. 2a), while the *E'* peak does not exhibit any noticeable trends (Fig. S3a). The frequency difference between the *A'* and *E'* peaks does increase from ~19.5 up to ~22 cm^{-1} as the PLE redshifts from ~1.84 to 1.81 eV (Fig. S3b). A redshift in the *A'* frequency has been observed previously in gated MoS_2 devices where simultaneous Raman and electrical transport measurements were performed.[31] Interestingly, the *E'* peak does not exhibit strong frequency shifts upon gating and this insensitivity to doping is a result of weaker electron phonon coupling compared to the *A'* mode.[31]

By comparing our data to Ref. [31], we can get an estimate of the charge densities in our samples. In their gated device experiments, Ref. [31] established the dependence of the *A*' peak frequency on electron density to be -2.22 x 10^{13} cm. We use this relationship to calculate the charge densities corresponding to our measured *A*' peak frequencies. While we do not know the exact *A*' frequency for pristine undoped MoS_2 in our sample, we can still calculate relative changes in electron density and thereby obtain order-of-magnitude estimates of electron densities. We therefore assume the highest *A'* frequency (404.6 cm^{-1}, corresponding to a PLE of 1.84 eV) to be that of undoped MoS_2, i.e. zero charge, and calculate electron densities corresponding to the rest of the *A'* frequencies using the above relation. A plot of the PLE against the extracted electron densities (*n*) is shown in Fig. 2b. The calculated electron densities reach a maximum of ~7 x 10^{12} cm^{-2}, lower than the charges injected in the gated MoS_2 experiments[31], but similar to previous

measurements of carrier concentration in defective MoS_2.[32] Our study therefore shows an easy way to estimate carrier concentration by combining PL with Raman spectroscopy. We also plot the $I_{LA}/I_{E'}$ ratios against *n* in Fig. 2c, which shows an increase in the defect-induced *LA* peak with increasing electron density.

Defect Passivation

Having established that the aged MoS_2 crystals exhibit redshifted PL, higher electron densities, and increasing intensities of the defect-induced Raman peak, all presumably due to sulfur vacancies, we next explore the passivation of these defects with *in situ* PL and Raman measurements. We subject several monolayer MoS_2 crystals to laser irradiation at varying power densities (ranging from 0.18 to 3.17 x 10^5 W/cm^{2,} and corresponding to laser powers ranging from 0.06 to 1.1 mW) and measure the evolution of the PLE and Raman spectra. These *in situ* measurements are performed at atmospheric pressure and under vacuum inside a commercial Raman microscope (Renishaw inVia microscope, 100x objective lens and 600 nm spot size). Similar to previous reports,[17,20] we find that laser irradiation causes an enhancement of PL intensity, and its spectral weight blueshifts over time. In our experiments the enhancement typically occurs below a power density of 2 x 10^5 W/cm^2 and is stable, i.e. the PL intensity remains high after the irradiation process. Higher powers result in a decrease in PL intensity although the PLE still exhibits a blueshift.

Figure 3 illustrates the changes in the electronic and vibrational properties upon irradiation at lower (Fig. 3a) and higher (Fig. 3b) power densities. When irradiated with a low power density (633 nm excitation at ~0.3 x 10^5 W/cm^2) the PL intensity increases over a duration of ~160s (bottom panel in Fig. 3a). The PLE blueshifts concomitantly by ~5 meV (middle panel in Fig. 3a). Since the excitation is 633 nm, we simultaneously monitor the evolution of the Raman peaks and find a decrease in the *LA* peak intensity over the duration of the experiment (top panel in Fig. 3a). The passivation kinetics curves exhibit a steep initial increase followed by a gradual increase after

which the curves stabilize to a final value. We find that the curves are best fit with a double exponential, with an initial shorter time constant and a second longer time constant. The time constants for the double exponential fit to both the PLE and $I_{LA}/I_{E'}$ curves in Figure 3a are 4 and 30s.

Figure 3b shows what happens at higher power densities (3.17 x 10^5 W/cm^2). The PL intensity drops rapidly as soon as the laser irradiation begins, while the emission energy blueshifts similar to the case of the low power irradiation. The blueshift of the PLE for several other irradiation experiments is shown in Fig. S4. The $I_{LA}/I_{E'}$ ratio exhibits a slight increase, corroborating the decrease in PL intensity and suggesting that the high laser irradiation causes an increase in defect density in the MoS_2 crystal. The corresponding Raman peaks do not shift significantly (Fig. S5) under low laser powers, but blueshift by ~3 cm^{-1} at higher laser powers (>3 x 10^5 W/cm^2). Notably, the Raman peaks do not redshift appreciably (within the ~1 cm^{-1} resolution of our spectrometer) as has been reported for laser irradiation at high power densities (up to 2 x 10^7 W/cm^2)[20] or long times,[17] indicating that there is no significant heating by the laser and that the irradiation is occurring at or close to room temperature.

Time constants calculated by fitting the $I_{LA}/I_{E'}$ curves for irradiation at various power densities are shown in Fig. 4a. Understandably, the time constants decrease with increasing laser power. Note that Fig. 4a only shows time constants corresponding to power densities less than 2 x 10^5 W/cm^2 since we observe a decline in PL intensity, increase in defect density (Fig. 3b) and blueshifted Raman peaks (Fig. S5) for irradiation at higher laser power densities. In addition to the dependence of time constants on the power density, we also calculate the change in electron density before and after laser irradiation by comparing the blueshifts of the PLE (Fig. S4) to the PLE versus electron density plot in Fig. 2b. The results are plotted in Fig. 4b, which shows the calculated Δn against laser power density, where Δn is the difference between the PLE energy after laser irradiation and the initial PLE energy. The negative values of Δn correspond to a decrease in electron density, or p-type doping caused by the adsorption and bonding of oxygen

to the MoS_2. Moreover, Δn clearly increases with increasing laser power density by a factor of ~3. The scatter in the data in Fig. 4b arise from the different initial PLE energies in the crystals, which in turn depend on their initial defect densities (sulfur vacancies).

To gain further insight into the passivation mechanism, we compare the kinetics of passivation at atmospheric pressure and in vacuum. The low-pressure experiments are performed in a standard environmental microscope stage (Linkam Scientific) that is evacuated to its base pressure (~10^{-3} torr). Examples of laser irradiation at low power density (~0.2 x 10^5 W/cm^2) under vacuum are shown in Figures 5a and 5b, which plot the temporal evolution PL intensity and PLE energy, respectively. For comparison we also include a passivation kinetics curve collected using the same power density at atmospheric pressure. We find that the passivation in vacuum also follows similar trends as in atmospheric pressure, i.e. increase in PL intensity (bottom panel in Fig. 5a) and blueshift of the PLE (bottom panel in Fig. 5b). We attribute the blueshift and increase to residual oxygen that is present in the chamber. However, the shape of the kinetics curve is different, and the curve can be fit with a single exponential (with a time constant ~45 s) rather than a double exponential (with time constants ~7 and ~500 s) in the case of atmospheric pressure irradiation (top panels in Figs. 5a and 5b).

The differences in kinetics between atmospheric and low pressure irradiation suggest that the evacuation of the chamber removes organic surface adsorbates that are naturally present on the MoS_2 layers and that this step is followed by the oxygen passivation (adsorption), resulting in a single-step (single-exponential) passivation curve. On the other hand, the laser in the atmospheric pressure experiments rapidly irradiates the surface adsorbates, followed by the more gradual step of oxygen passivation. This results in the two-step, double exponential passivation curve during atmospheric pressure laser irradiation. Furthermore, the dependence of the time constants on the laser power density (Fig. 4a) indicates that the initial step of adsorbate removal by the laser is faster for higher power densities (lower time constants). With increasing laser power, the rapid removal of surface adsorbates is followed by rapid oxygen adsorption into the

sulfur vacancies, also resulting in lower time constants. The role of the laser therefore appears to be primarily to clean the surface of the MoS_2 and allowing the oxygen molecules to adsorb over the layer exponentially over time. This process is shown schematically in Fig. 5c.

Atomic force microscopy does not reveal any discernable differences (within the resolution of our instrument) in the topography before and after irradiation (Fig. S6), suggesting that the enhancement occurs at the atomic level. Low-temperature PL experiments do provide some more understanding into the atomic-level passivation process. These experiments are performed at 77K in a nitrogen ambient, which is known to enhance an excitonic emission peak ~0.1 eV lower than the *A* and A^- exciton emission energies.[6] This peak has been attributed to emission from excitons bound to lattice defects (X^B) in monolayer TMDs.[6,33-35] Figure 6 shows an example of the effect of laser irradiation on the bound exciton peak intensity. The bottom spectrum in the waterfall plot in Fig. 6 contains 3 distinct peaks that are labeled in the figure. In addition to the A and B exciton peaks, there appears a broad peak centered at ~1.7 eV, which can be attributed to exciton emission bound to defects (X^B). The X^B peak is asymmetric, and it could be composed of at least two sub-peaks, which appear due to emission of excitons bound to mono- and di-sulfur vacancies, as reported recently.[35] Upon laser irradiation at 77K (excitation at 514 nm, power density 0.32 x 10^5 W/cm^2), the X^B peak intensity clearly decreases and almost completely disappears in less than 30s. The inset in Fig. 6 shows the decrease in the intensity of the X^B peak relative to the *A* exciton peak. In addition to the changes in relative intensities, the overall intensity of the *A* exciton peak increases as the X^B peak decreases. This can be seen clearly in Fig. S6a where the spectra are overlaid on to one another. Furthermore, the *A* exciton peak exhibits a small redshift upon laser irradiation, possibly due to an increase in electron density upon irradiation. Similar laser irradiation experiments on several other monolayer MoS_2 crystals shows varying initial intensities of the X^B peak but in all experiments the X^B peak intensity decreases over the duration of laser irradiation (see Fig. S6b for another example of decreasing X^B peak intensity under laser

irradiation at 77 K). In addition to the decrease in X^B peak intensity, we also observe a decrease in the defect density when 633 nm excitation is used (Fig. S6c).

Our observation of bound excitons at low temperature and the decrease in intensity of bound exciton emission agrees very well with the room temperature observation of enhanced PL intensity. Furthermore, the *in situ* PL measurements correlate with changes in the *in situ* Raman spectra where the laser irradiation causes a decrease in the defect-related *LA* peak.

Conclusions

In conclusion, we have shown that lattice defects in CVD-grown MoS_2 cause a redshift and broadening of the excitonic photoemission. Low temperature PL measurements also show the presence of excitons bound to defects. These defects produce an increase in scattering of electrons by zone boundary *LA* phonons, which correlate very well with the PL measurements. We attribute these defects to sulfur vacancies, which are known to be the most common lattice defects in MoS_2. By comparing with previous reports, we estimate the resultant increase in electron density to be up to 7×10^{12} cm^{-2} . The vacancies can be passivated by the adsorption and bonding of oxygen. *In situ* PL and Raman measurements show that the passivation process is aided by laser irradiation (at low or moderate power densities) wherein the laser first removes surface adsorbates (fast kinetics), followed by oxygen bonding at the vacancy sites (slow kinetics). The irradiation reduces the electron density in the MoS_2 and the laser power density can modulate the carrier concentration. Our study provides deeper understanding into the ambient laser-mediated passivation process and shows a simple way to passivate tune the electronic properties of monolayer MoS_2. This approach can be easily extended to all monolayer TMDs that have an affinity to bonding with oxygen.

Acknowledgements

The authors gratefully acknowledge funding from the Air Force Office of Scientific Research.

References

(1) Wang, Q. H.; Kalantar-Zadeh, K.; Kis, A.; Coleman, J. N.; Strano, M. S. Electronics and Optoelectronics of Two-Dimensional Transition Metal Dichalcogenides. *Nature Nanotech.* **2012**, *7*, 699-712.

(2) Bhimanapati, G. R.; Lin, Z.; Meunier, V.; Jung, Y.; Cha, J. J.; Das, S.; Xiao, D.; Son, Y.; Strano, M. S.; Cooper, V. R. Recent Advances in Two-Dimensional Materials Beyond Graphene. *ACS nano* **2015**.

(3) Bernardi, M.; Ataca, C.; Palummo, M.; Grossman, J. C. Optical and Electronic Properties of Two-Dimensional Layered Materials. *Nanophotonics* **2017**, *6*, 479-493.

(4) Splendiani, A.; Sun, L.; Zhang, Y.; Li, T.; Kim, J.; Chim, C.-Y.; Galli, G.; Wang, F. Emerging Photoluminescence in Monolayer Mos2. *Nano Lett.* **2010**, *10*, 1271-1275.

(5) Gutierrez, H. R.; Perea-Lopez, N.; Elías, A. L.; Berkdemir, A.; Wang, B.; Lv, R.; López-Urías, F.; Crespi, V. H.; Terrones, H.; Terrones, M. Extraordinary Room-Temperature Photoluminescence in Ws2 Triangular Monolayers. *Nano Lett.* **2012**, *13*, 3447-3454.

(6) Tongay, S.; Suh, J.; Ataca, C.; Fan, W.; Luce, A.; Kang, J. S.; Liu, J.; Ko, C.; Raghunathanan, R.; Zhou, J.*et al.* Defects Activated Photoluminescence in Two-Dimensional Semiconductors: Interplay between Bound, Charged, and Free Excitons. *Sci. Rep.* **2013**, *3*.

(7) Zhou, W.; Zou, X.; Najmaei, S.; Liu, Z.; Shi, Y.; Kong, J.; Lou, J.; Ajayan, P. M.; Yakobson, B. I.; Idrobo, J.-C. Intrinsic Structural Defects in Monolayer Molybdenum Disulfide. *Nano Lett.* **2013**, *13*, 2615-2622.

(8) Hong, J.; Hu, Z.; Probert, M.; Li, K.; Lv, D.; Yang, X.; Gu, L.; Mao, N.; Feng, Q.; Xie, L.*et al.* Exploring Atomic Defects in Molybdenum Disulphide Monolayers. *Nat. Commun.* **2015**, *6*, 6293.

(9) Lin, Z.; Carvalho, B. R.; Kahn, E.; Lv, R.; Rao, R.; Terrones, H.; Pimenta, M. E.; Terrones, M. Defect Engineering of Two-Dimensional Transition Metal Dichalcogenides. *2D Mater.* **2016**.

(10) Cho, K.; Min, M.; Kim, T.-Y.; Jeong, h.; Pak, J.; Kim, J.-K.; Jang, J.; Yun, S. J.; Lee, Y. H.; Hong, W.-K.*et al.* Electrical and Optical Characterization of Mos2 with Sulfur Vacancy Passivation by Treatment with Alkanethiol Molecules. *ACS Nano* **2015**, *9*, 8044-8053.

(11) Sim, D. M.; Kim, M.; Yim, S.; Choi, M.-J.; Choi, J.; Yoo, S.; Jung, Y. S. Controlled Doping of Vacancy-Containing Few-Layer Mos2 Via Highly Stable Thiol-Based Molecular Chemisorption. *ACS Nano* **2015**, *9*, 12115-12123.

(12) Amani, M.; Lien, D.-H.; Kiriya, D.; Xiao, J.; Azcatl, A.; Noh, J.; Madhvapathy, S. R.; Addou, R.; Santosh, K.; Dubey, M. Near-Unity Photoluminescence Quantum Yield in Mos2. *Science* **2015**, *350*, 1065-1068.

(13) Han, H.-V.; Lu, A.-Y.; Lu, L.-S.; Huang, J.-K.; Li, H.; Hsu, C.-L.; Lin, Y.-C.; Chiu, M.-H.; Suenaga, K.; Chu, C.-W.*et al.* Photoluminescence Enhancement and Structure Repairing of Monolayer Mose2 by Hydrohalic Acid Treatment. *ACS Nano* **2016**, *10*, 1454-1461.

(14) Alharbi, A.; Zahl, P.; Shahrjerdi, D. Material and Device Properties of Superacid-Treated Monolayer Molybdenum Disulfide. *Appl. Phys. Lett.* **2017**, *110*, 033503.

(15) Nan, H.; Wang, Z.; Wang, W.; Liang, Z.; Lu, Y.; Chen, Q. Strong Photoluminescence Enhancement of Mos2 through Defect Engineering and Oxygen Bonding. *ACS Nano* **2014**, *8*, 5738-5745.

(16) Shu, H.; Li, Y.; Niu, X.; Wang, J. Greatly Enhanced Optical Absorption of a Defective Mos2 Monolayer through Oxygen Passivation. *ACS Appl. Mater. Interfaces* **2016**, *8*, 13150-13156.

(17) Oh, H. M.; Han, G. H.; Kim, H.; Bae, J. J.; Jeong, M. S.; Lee, Y. H. Photochemical Reaction in Monolayer Mos2 Via Correlated Photoluminescence, Raman Spectroscopy, and Atomic Force Microscopy. *ACS Nano* **2016**, *10*, 5230-5236.

(18) Ko, P. J.; Abderrahmane, A.; Thu, T. V.; Ortega, D.; Takamura, T.; Sandhu, A. Laser Power Dependent Optical Properties of Mono-and Few-Layer Mos2. *J. Nanosci. Nanotech.* **2015**, *15*, 6843-6846.

(19) Tongay, S.; Zhou, J.; Ataca, C.; Liu, J.; Kang, J. S.; Matthews, T. S.; You, L.; Li, J.; Grossman, J.; Wu, J. Broad-Range Modulation of Light Emission in Two-Dimensional Semiconductors by Molecular Physisorption Gating. *Nano Lett.* **2013**, *13*, 2831-2836.

(20) Lu, J.; Carvalho, A.; Chan, X. K.; Liu, H.; Liu, B.; Tok, E. S.; Loh, K. P.; Castro Neto, A. H.; Sow, C. H. Atomic Healing of Defects in Transition Metal Dichalcogenides. *Nano Lett.* **2015**, *15*, 3524-3532.

(21) Rao, R.; Islam, A. E.; Campbell, P. M.; Vogel, E. M.; Maruyama, B. In Situ Thermal Oxidation Kinetics in Few Layer Mos2. *2D Mater.* **2017**, *4*, 025058.

(22) Islam, A. E.; Kim, S. S.; Rao, R.; Ngo, Y.; Jiang, J.; Nikolaev, P.; Naik, R. R.; Pachter, R.; Boeckl, J.; Maruyama, B. Photothermal Oxidation of Single Layer Graphene. *RSC Advances* **2016**.

(23) He, Z.; Wang, X.; Xu, W.; Zhou, Y.; Sheng, Y.; Rong, Y.; Smith, J. M.; Warner, J. H. Revealing Defect-State Photoluminescence in Monolayer Ws2 by Cryogenic Laser Processing. *ACS Nano* **2016**, *10*, 5847-5855.

(24) Gao, J.; Li, B.; Tan, J.; Chow, P.; Lu, T.-M.; Koratkar, N. Aging of Transition Metal Dichalcogenide Monolayers. *ACS Nano* **2016**, *10*, 2628-2635.

(25) Mouri, S.; Miyauchi, Y.; Matsuda, K. Tunable Photoluminescence of Monolayer Mos 2via Chemical Doping. *Nano Lett.* **2013**, *13*, 5944-5948.

(26) Mao, N.; Chen, Y.; Liu, D.; Zhang, J.; Xie, L. Solvatochromic Effect on the Photoluminescence of Mos 2monolayers. *Small* **2013**, *9*, 1312-1315.

(27) Molina-Sánchez, A.; Wirtz, L. Phonons in Single and Few-Layer Mos2 and Ws2. *Phys. Rev. B* **2011**, *84*, 155413.

(28) Frey, G. L.; Tenne, R.; Matthews, M. J.; Dresselhaus, M. S. Raman and Resonance Raman Investigation of Mos2 Nanoparticles. *Phys. Rev. B* **1999**, *60*, 2883-2892.

(29) McDevitt, N. T.; Zabinski, J. S.; Donley, M. S.; Bultman, J. E. Disorder-Induced Low-Frequency Raman Band Observed in Deposited Mos2 Films. *Appl. Spec.* **1994**, *48*, 733-736.

(30) Mignuzzi, S.; Pollard, A. J.; Bonini, N.; Brennan, B.; Gilmore, I. S.; Pimenta, M. A.; Richards, D.; Roy, D. Effect of Disorder on Raman Scattering of Silgle-Layer Mos2. *Phys. Rev. B* **2015**, *91*, 195411.

(31) Chakraborty, B.; Bera, A.; Muthu, D. V. S.; Bhowmick, S.; Waghmare, U. V.; Sood, A. K. Symmetry-Dependent Phonon Renormalization in Monolayer Mos2 Transistor. *Phys. Rev. B* **2012**, *85*, 161403(R).

(32) Qiu, H.; Xu, T.; Wang, Z.; Ren, W.; Nan, H.; Ni, Z.; Chen, Q.; Yuan, S.; Miao, F.; Song, F.*et al.* Hopping Transport through Defect-Induced Localized States in Molybdenum Disulphide. *Nat. Commun.* **2013**, *4*, 2642.

(33) Carozo, V.; Wang, Y.; Fujisawa, K.; Carvalho, B. R.; McCreary, A.; Feng, S.; Lin, Z.; Zhou, C.; Perea-López, N.; Elías, A. L.*et al.* Optical Identification of Sulfur Vacancies: Bound Excitons at the Edges of Monolayer Tungsten Disulfide. *Science Advances* **2017**, *3*.

(34) Chow, P. K.; Jacobs-Gedrim, R. B.; Gao, J.; Lu, T.-M.; Yu, B.; Terrones, H.; Koratkar, N. Defect-Induced Photoluminescence in Monolayer Semiconducting Transition Metal Dichalcogenides. *ACS Nano* **2015**, *9*, 1520-1527.

(35) Saigal, N.; Ghosh, S. Evidence for Two Distinct Defect Related Luminescence Features in Monolayer Mos2. *Appl. Phys. Lett.* **2016**, *109*, 122105.

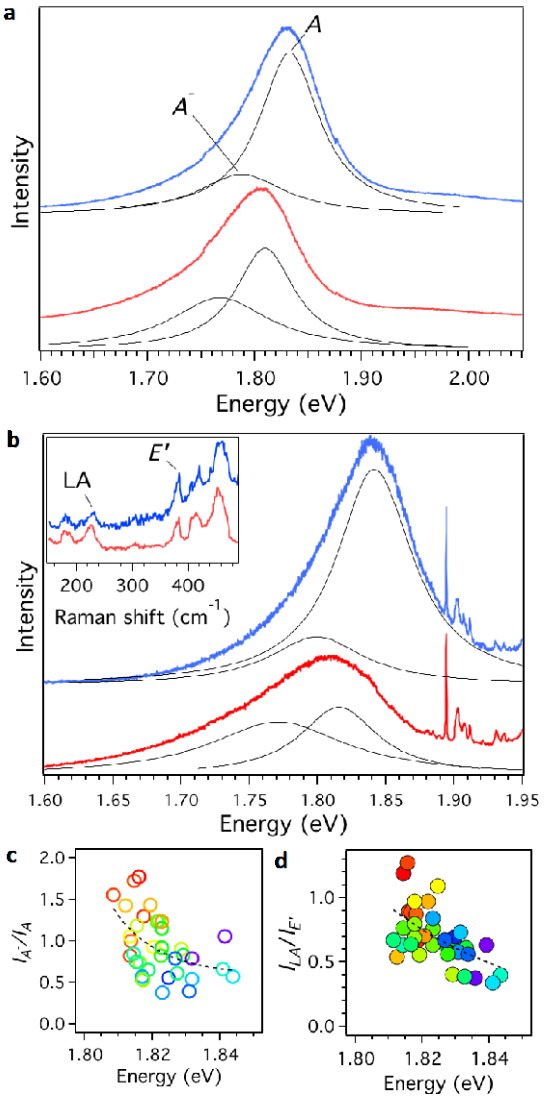

Figure 1. Optical characterization of aged monolayer MoS_2 crystals with defects. PL emission spectra collected with (a) 514 nm, and (b) 633 nm excitation. All spectra have been normalized with respect to the Raman peak of the Si substrate and fitted with Lorentzian peaks after baseline subtraction. The inset in (b) displays the same spectra but plotted as Raman shift. The defect-induced *LA* peak at ~225 cm^{-1} is more intense in the lower (red) trace, which also exhibits increased trion emission (A^- peak). (c) Intensity ratio (I_{A^-}/I_A) between the trion (A^-) and bi-exciton (A) peaks plotted against the average PL emission energy (514 nm excitation). (d) $I_{LA}/I_{E'}$ plotted against average PL emission energy (633 nm excitation), showing that increased trion emission corresponds to an increase in intensity of the defect-induced *LA* peak. The dashed lines in (c) and (d) are guides to the eye.

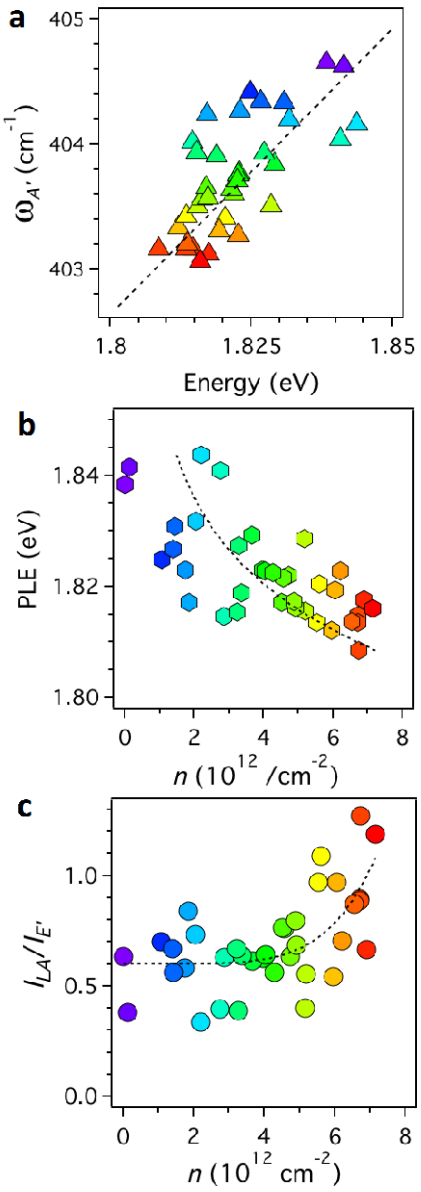

Figure 2. Relationships between optical data and electron densities. (a) *A'* peak frequencies plotted against the PL emission energies (excitation at 514 nm). The inset shows the reduced peak frequencies

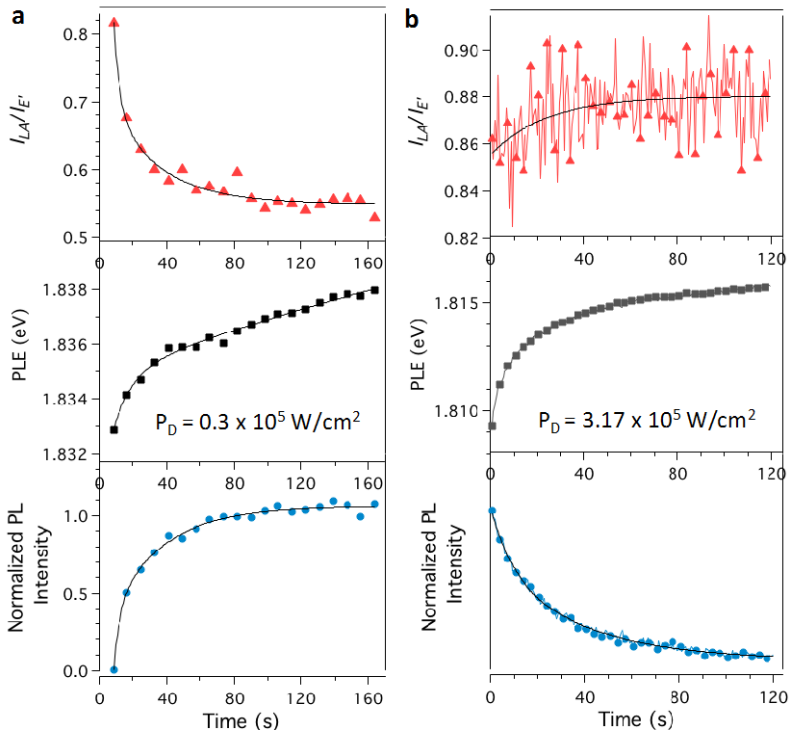

Figure 3. Defect passivation kinetics. (a) Effect of low power laser irradiation (P_D = 0.3 x 10^5 W/cm^2) on the PL Intensity (bottom panel), PLE (middle panel) and $I_{LA}/I_{E'}$ ratio over time. (b) Same as in (a) except laser irradiation performed at a higher power (P_D = 3.17 x 10^5 W/cm^2). Low power densities enhance the PL intensity and lower the defect density, whereas high power densities result in the opposite effect.

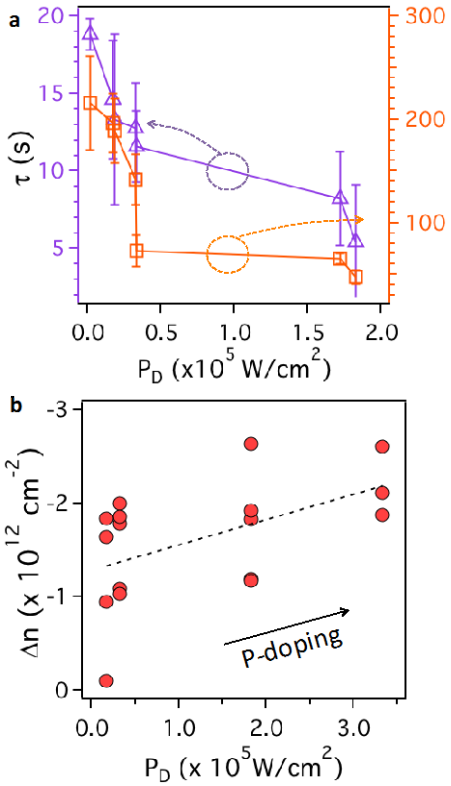

Figure 4. Effect of laser power density on passivation kinetics and carrier density. (a) Average time constants obtained from fitting of several passivation kinetics curves to a double exponential function, plotted against the power density (P_D). Both short and long time constants are plotted on the left and right y-axis, respectively. Only P_D values less than 2 x 10^5 W/cm^2 are considered due to degradation of the PL intensity at higher powers. (b) Difference in charge densities before and after the laser irradiation process. The electron density values are obtained by comparing the PLE energy to the calculated n values in Fig. 2b. Negative values for Δn indicate a decrease in electron density after laser irradiation, or p-doping of the MoS2. The figure indicates that the carrier density can be modulated by a factor of 3 by tuning the laser power density in the presence of oxygen.

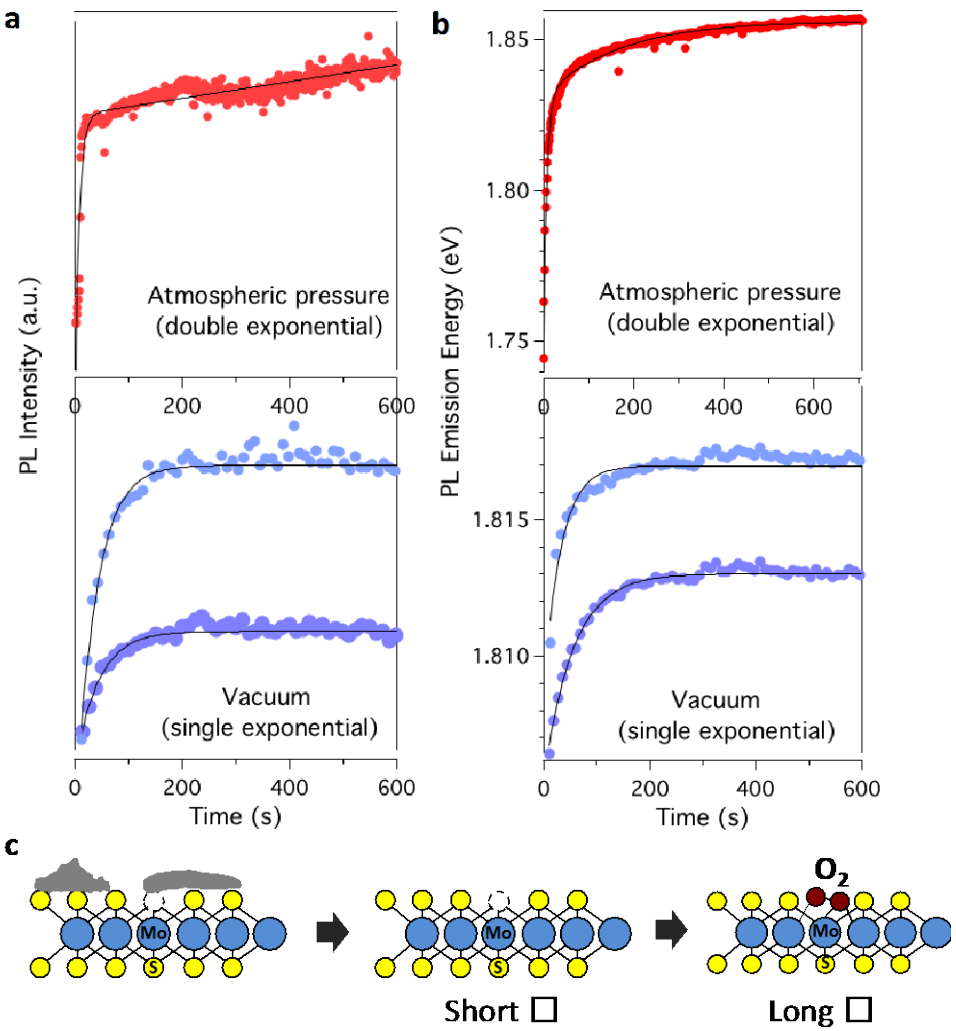

Figure 5. Comparison between passivation kinetics in vacuum and atmospheric pressure. (a) Evolution of PL intensity over time in laser irradiation experiments performed under vacuum (bottom panel) and at atmospheric pressure (top panel). Two different examples are shown for the vacuum experiments, corresponding to two different MoS_2 crystals. (b) Same as in (a) except evolution of the corresponding PLE. The kinetics curves can be fit to a single exponential for the vacuum experiments, while a double exponential fit is needed to fit the atmospheric pressure data. The fits highlight the mechanistic differences between vacuum and atmospheric pressure (see text for more details). (c) Schematic showing the process of defect passivation by laser irradiation. As-grown MoS2 contains lattice defects and surface adsorbents that are removed by the laser rapidly at the onset of irradiation. This step has a short lifetime (<10 s)

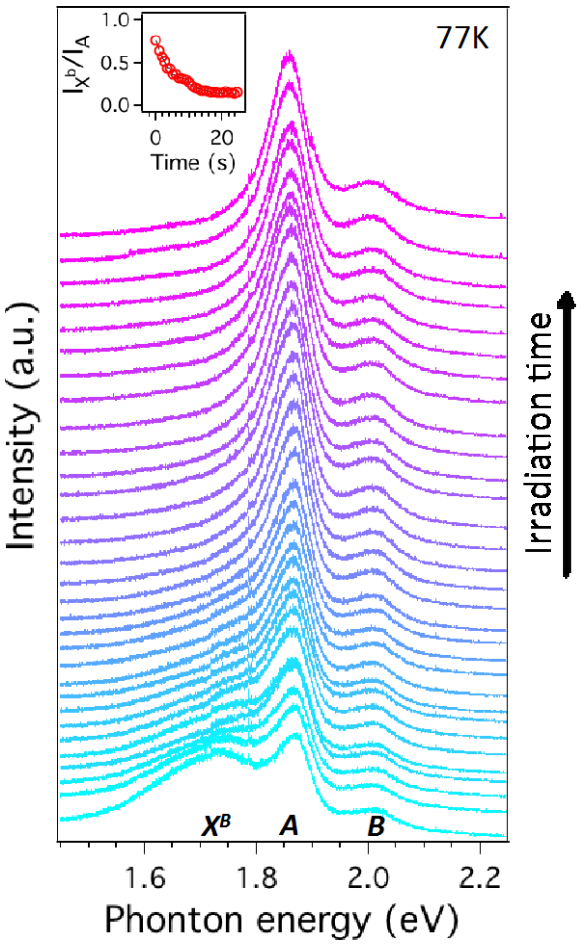

Figure 6. Low temperature PL (77K) spectra showing evolution of exciton peaks over the duration of a laser irradiation experiment (excitation 514 nm, power density 0.32 x 10^5 W/cm^2. The spectra (normalized to the Si Raman peak intensity) are plotted as a waterfall plot, with increasing irradiation time from bottom to top. Three exciton emission peaks are observed and labeled in the bottom spectrum as X^B, *A* and *B*, centered at 1.7, 1.85 and 2 eV, respectively. The X^B peak corresponds to exciton emission bound to defects, and its intensity decreases over laser irradiation time (< 30s). The decrease can be seen clearly in the inset, which plots the intensity of the X^B peak relative to the *A* exciton peak intensity.

Supplementary Information

Passivation of Defects in Monolayer MoS_2 – In situ Photoluminescence and Raman Studies

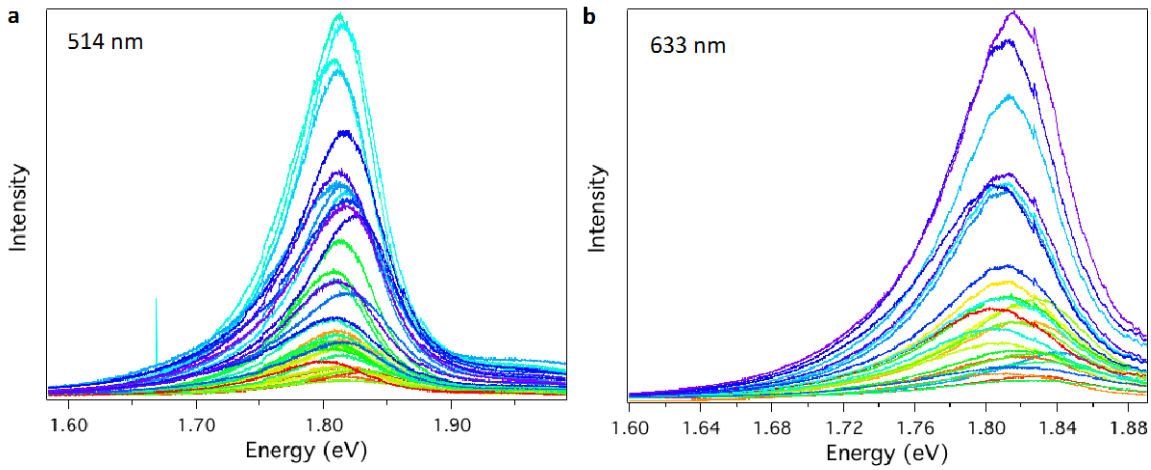

Figure S1. PLE spectra collected using (a) 514 nm, and (b) 633 nm excitation from 40 different CVD-grown monolayer MoS_2 crystals on SiO_2. All spectra have been normalized with respect to the Raman peak from the Si substrate.

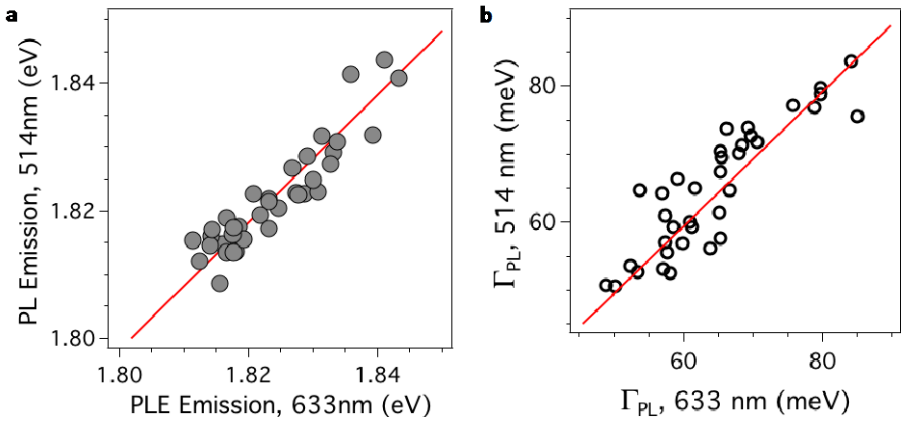

Figure S2. Equivalence between 514 and 633 nm data.(a) PL emission energies using 514 nm excitation plotted against PL emission energies using 633 nm excitation. Each data point corresponds to a monolayer MoS_2 crystal that has been irradiated at the same spot with both laser excitations. (b) Width of the PL emission peaks using 514 nm excitation plotted against width of the PL emission peaks using 633 nm excitation. The widths are obtained by fitting a single Lorentzian peak to the emission curves. The data sets can be fit to a straight line with slope = 1, making it possible to compare the 514nm and 633nm data.

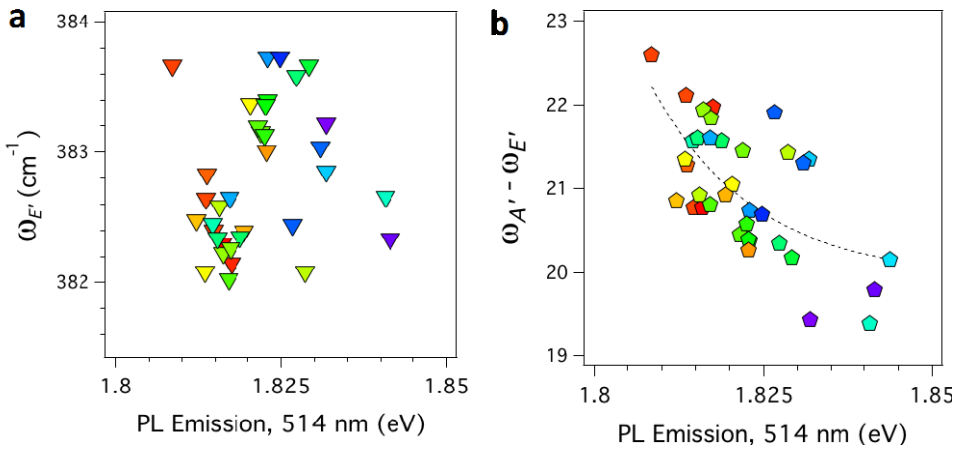

Figure S3. (a) Frequencies of the *E'* Raman peak plotted against the PLE energies. Unlike the *A'* peak, the *E'* peak does not exhibit a strong frequency dependence on the PLE energy. (b) Frequency difference between the *A'* and *E'* Raman peaks, plotted against PLE energies.

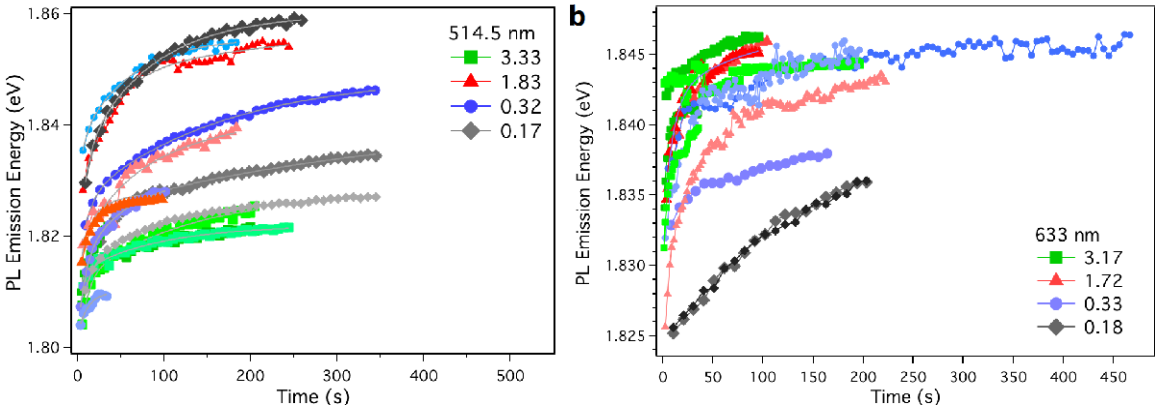

Figure S4. Variation of PLE with laser power density (x 10^5 W/cm^2) for (a) 514 nm, and (b) 633 nm excitation.

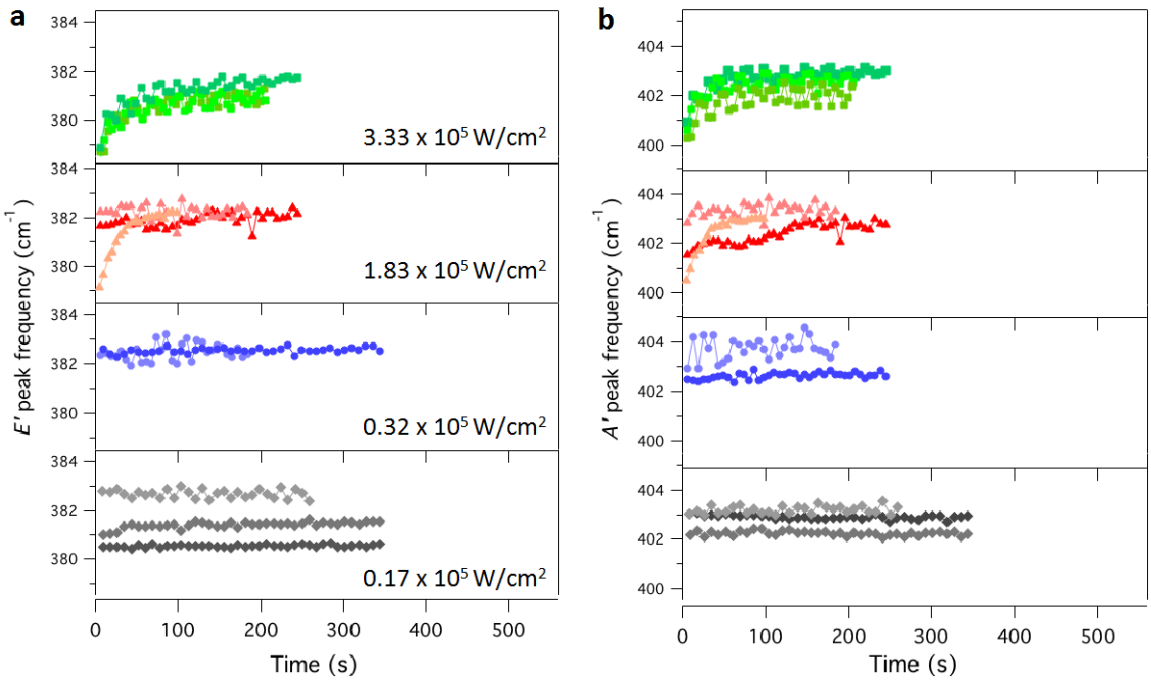

Fig. S5 – Temporal variation of the (a) *E'*, and (b) *A'* Raman frequencies for different laser irradiation power densities (514 nm excitation). The peak frequencies do not shift significantly for low laser power densities (up to 0.32 x 10^5 W/cm^2) and exhibit blueshifts over time at higher power densities. Multiple traces in the figure correspond to irradiation at different spots.

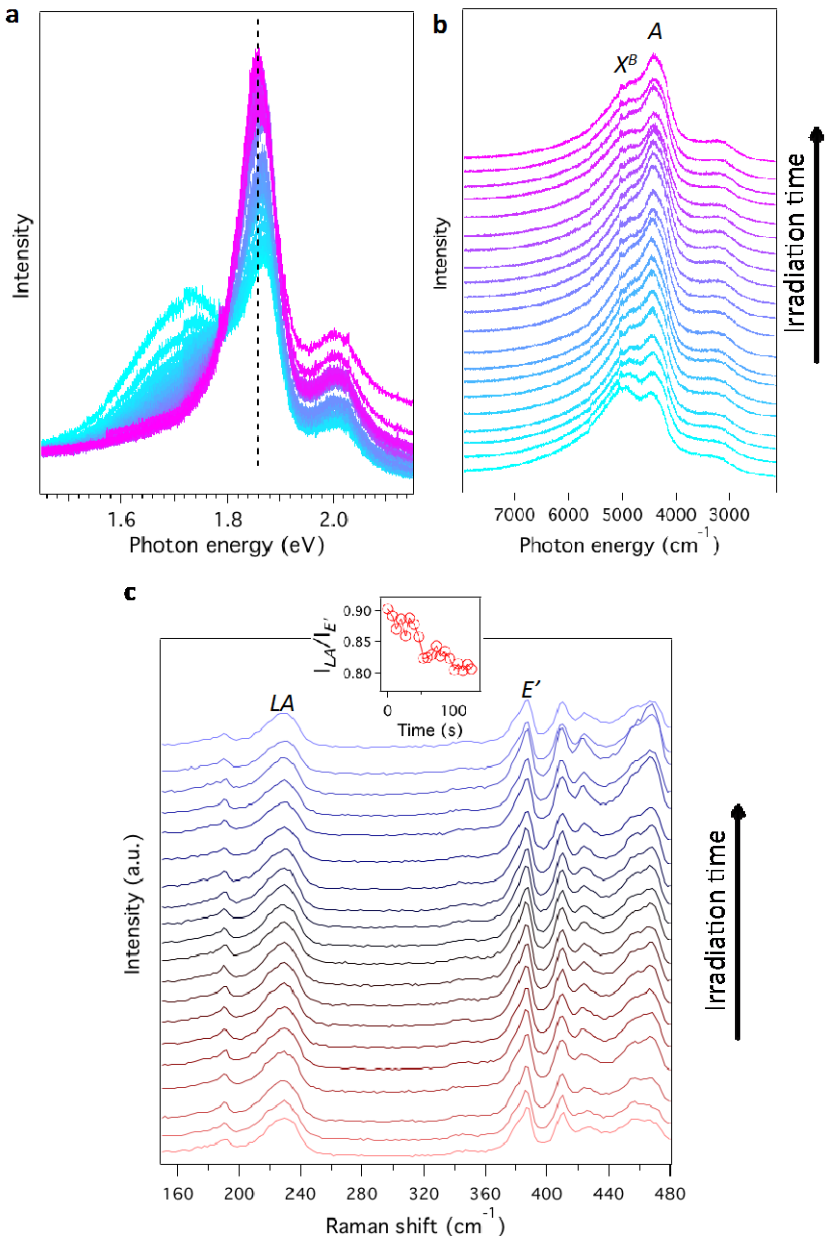

Figure S6. (a) The same spectra as in Fig. 6 in the main manuscript, except that they are overlaid on top of each other. The enhancement of the *A* exciton peak intensity upon laser irradiation at 77K can be seen clearly. (b) Low-temperature PL spectra (excitation at 514 nm) collected at a different spot (crystal), also showing a decrease in the bound exciton (X^B) peak intensity over time. (c) Resonance Raman spectra (633 nm excitation) collected at 77K, showing a small but clear decrease in the intensity of the defect-induced *LA* peak. The inset shows the decrease in *LA* peak intensity relative to the *E'* peak intensity over time.

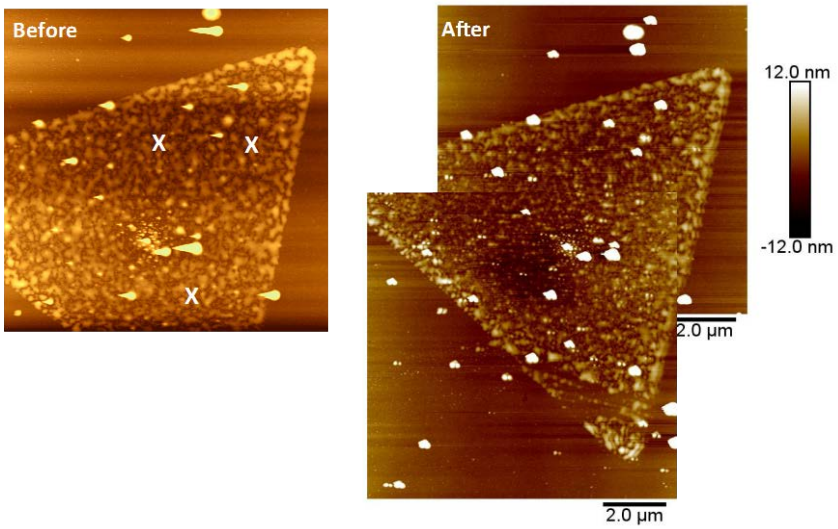

Figure S7. Atomic force microscope images of a monolayer MoS_2 crystal that has undergone laser irradiation at several spots (indicated by X). No discernable difference before and after irradiation can be seen within the resolution of the AFM image.